Materials Research. 2025; 28: e20250399
DOI: https://doi.org/10.1590/1980-5373-MR-2025-0399

A Comparative Study on the Electrochemical Corrosion Behavior of WC-Ni-Si and WC-Co Cemented Carbides

***Flávio Amaury de Freitas Matos*[a], *Edmilson Otoni Corrêa*[a], *Nádia Alves Nery Balbino*[a], *Danilo Roque Huanca*[a]**

[a]*Universidade Federal de Itajubá, Av. BPS, 1303, Pinheirinho, Itajubá, MG, Brasil.*

Received: April 04, 2025; Revised: July 15, 2025; Accepted: August 16, 2025

This study investigates the microstructure and corrosion behavior of WC-NiSi cemented carbide produced by conventional powder metallurgy, with comparative analysis against traditional WC-Co cemented carbide. Microstructural characterization was carried out using scanning electron microscopy (SEM), energy-dispersive X-ray spectroscopy (EDS), and X-ray diffraction (XRD) before and after corrosion testing. Electrochemical performance was evaluated in a 3.5 wt.% NaCl solution through open-circuit potential (OCP) measurements, linear potentiodynamic polarization, and electrochemical impedance spectroscopy (EIS). The WC-NiSi cemented carbide exhibited a microstructure similar to WC-Co, although with a slightly higher porosity and increased presence of binder islands. Electrochemical assessments revealed that the cemented carbide with NiSi binder demonstrated more noble corrosion potentials, reduced current density, and higher overall impedance compared to its Co binder counterpart, indicating enhanced corrosion resistance.

Keywords: *Cemented carbides, corrosion, potentiodynamic polarization, electrochemical impedance spectroscopy.*

1. Introduction

Cemented carbide of tungsten consists of a large fraction of WC particles (hard phase) embedded in a low-melting metal or metal alloy binder. It mostly uses cobalt as the metal binder due to its excellent wetting and adhesion and it is widely known by its high hardness, high strength and exceptional wear resistance. The combination of these properties allows its use in several applications such as cutting tools, drills, components of oil and gas drilling equipment, forming dies, wear-resistant components, balls for high-energy milling, sealing rings, coatings, valves, jet nozzles, saw blades, fluid mixers and conveyor belt scrapers among others[1-2].

However, there are significant reasons to substitute the cobalt as a metal binder in this material: (a) cobalt is a high-priced commodity; (b) cobalt is a toxic element, posing risks to handlers in various engineering applications where its powder or vapor is produced and (c) the low corrosion resistance of WC-Co cemented carbides[3].

Concerning to the low corrosion resistance of the WC-Co cemented carbide, it is worthwhile pointing out that in many applications of this material, which require wear resistance, the components are also in contact with chemically aggressive environments and corrosion can play an important role in surface degradation and significantly accelerate material wear[4].

In this sense, important research efforts have been targeted at finding an adequate alternative binder phase to replace cobalt that can improve the corrosion resistance of the cemented carbide of tungsten without sacrificing considerably its mechanical properties. Literature has reported that a binder alloy composed of nickel strengthened with other alloying elements such as silicon, by solid solution, may be a good solution for overcoming this deficiency[5-9].

The objective of this study is, therefore, to evaluate the microstructure and corrosion behavior of WC-NiSi compared to WC-Co cemented carbides, processed by conventional powder metallurgy.

2. Materials and Methods

The chemical compositions of the cemented carbide samples utilized in this study are presented in Table 1. The powders used for sample preparation are as follows:

- tungsten carbide and cobalt powder (WC-Co) with an average particle size of 3.0 μm;
- tungsten carbide (WC) powder with an average particle size of 2.5 μm;
- carbon with a maximum particle size of 2 μm;
- silicon carbide with an average particle size of 1 μm and a purity of 99%.

The procedure for preparation of the materials was based on the work of Correa et al.[3]. After the alloys were weighed into the desired fractions according to the compositions shown in Table 1, the powders were mixed in heptane in a cemented carbide-coated ball mill with a ball to powder weight ratio of 2:1 during 80 hours at a horizontal rotation speed of 50 rpm. Then, 1.75% by weight of paraffin was added to the mixture to improve its compaction. The samples were compacted in a stainless steel matrix, with a pressure of 130 MPa for 3 min.

*e-mail: *flavioeme@yahoo.com.br*
Associate Editor: Aloisio Klein.
Editor-in-Chief: Luiz Antonio Pessan.

Then, the paraffin was removed from the compacts at 500 °C, using a furnace with a tubular alumina chamber under a flow of hydrogen with slow heating. After one hour at 500 °C, the samples were heated to a temperature of 750 °C, remaining at this temperature for 30 minutes so that pre-sintering of the compacts could occur. Finally, the samples were sintered at 1460 °C for 1 hour in a high vacuum atmosphere (2 to 6 · 10^{-5} bar).

2.1. Structural and microstructural characterization

The samples were polished with diamond suspensions and were examined before and after the potentiodynamic polarization tests using a ZEISS scanning electron microscope (model EVO MA 15) with a Bruker electron energy dispersive spectrometer (model xFlash 360) coupled. Additionally, X-ray diffraction analysis was carried out using a PanalyticalX'Pert Pro diffractometer, employing copper radiation (λ = 1.5405980 Å), a current of 40 mA, a voltage of 40 kV, and scanning angles (2θ) ranging from 10° to 100°, with a step size of 0.02° and a counting time of 0.5 seconds.

2.2. Corrosion measurements

Electrochemical tests were performed using a standard three-electrode cell configuration. A silver/silver chloride electrode ($Ag/AgCl/KCl_{3mol/L}$) served as the reference electrode, while a platinum wire, spirally wound, acted as the counter electrode. The working electrode samples were mounted on a Teflon holder shaped like a pipe, with brass wire ensuring electrical contact and an exposed surface area of 0.10 cm^2. To minimize external interference, the cell was housed inside of a Faraday Cage, and cables were grounded. All tests were conducted at room temperature (25 ± 2 °C) in naturally aerated saline solutions containing 3.5 wt.% sodium chloride (NaCl), prepared using analysis-grade reagents and distilled/deionized water. A Potentiostat/Galvanostat Autolab system (model PGSTAT302N), controlled by NOVA 2.1.4 software, was employed for the measurements. For reliability, three replicate experiments were conducted for each electrochemical test across all sample sets.

The open circuit potential (E_{OC}) behavior was monitored over a 4-hour period to assess the electrochemical stability of the samples. Linear potentiodynamic polarization tests were conducted by first establishing a steady-state OCP for one hour following immersion in the electrolyte. Subsequently, a potential sweep was applied from −500 mV to +1200 mV (vs. OCP) at a scan rate of 1 mV/s. EIS measurements were performed at the OCP after one hour of immersion, using a frequency range of 10 mHz to 10 kHz with a 10 mV (RMS) of sinusoidal perturbation. Data were collected at 10 points per decade to ensure sufficient resolution across the frequency spectrum.

3. Results and Discussion

3.1. Microstructural analysis

Figures 1 and 2 show the scanning electron micrographs of the polished surface of WC-Co and WC-NiSi cemented carbides. It is possible to note that they present a microstructure characteristic of conventional cemented carbides, with the faceted WC grains (light phase) surrounded by the binder (dark phase), which is uniformly distributed throughout the tungsten carbide matrix, with the presence of few and small pores and binder islands throughout the sample. The existence of the η phase and graphite in the structure was not identified through the micrographs. The presence of traces of silicon carbide particles that had not been dissolved was also not observed.

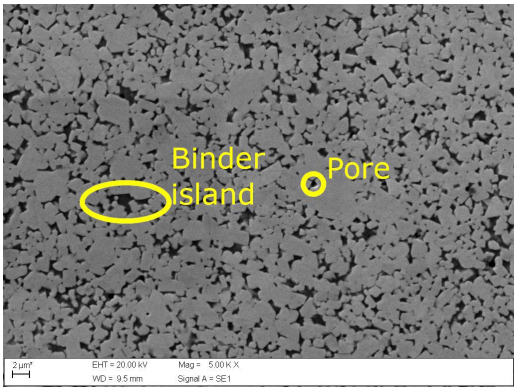

Figure 1. SEM image of the polished surface of the WC-Co cemented carbide.

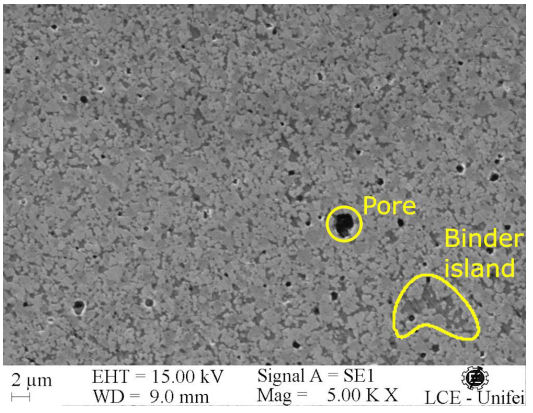

Figure 2. SEM image of the polished surface of the WC-NiSi cemented carbide.

Table 1. Chemical composition (wt.%) of cemented carbides.

Mixture composition						
Cemented carbide	% WC	% Binder	Binder composition			% C
			% Co	% Ni	% Si	
WC-Co	90	10	100	-	-	-
WC-NiSi	90	10	-	94.1	4.1	1.8

The results of the X-ray diffractograms (XRD) of the cemented carbides WC-Co and WC-NiSi are presented in Figure 3, in which the peaks of the hard phase (WC), the binder, nickel or cobalt, and the η phase can be seen. The peaks of the hard phase WC appear with greater intensity and quantity in all samples, as seen in the micrographs, it is the predominant phase in the microstructures. The peaks of the binder phases are identified by the elements in greater quantity in each binder (cobalt and nickel). As for the peaks identified as η phase, of low intensity, there is a difficulty in comparing them with the characteristic peaks of this phase, and their presence was also not observed in the microstructural analysis. This is probably due to the phase being finely dispersed in the material and with a low volume concentration or that these peaks were caused by XRD noise[1,10,11].

The chemical composition results obtained by EDS of the WC-Co and WC-NiSi cemented carbides are shown in Table 2. Compared with the values of the compositions of the raw materials, it is observed that there were no considerable losses for the WC-Co sample in the production process. For the WC-NiSi sample, there was an increase in the binder content, with a considerable variation in the nickel content, in relation to the initial composition of the raw material. However, it should be noted that these values are not very reliable because tungsten fluorescence influences the quantification of other elements, mainly nickel and chromium[12]. Therefore, due to the limitations of the method, the analyses are considered semi-quantitative and indicate only a trend and not the exact values of the concentrations of the elements[13].

According to Table 2, only traces of Si were observed, which supports the reasonable assumption that silicon was mostly, as desired, solubilized in the nickel.

3.2. Electrochemical analysis

3.2.1 Open circuit potential

The open-circuit potential (OCP) curves of WC-Co and WC-NiSi samples are shown in Figure 4. The WC-NiSi sample initially exhibits anodic corrosion behavior during potential stabilization, with the potential gradually decreasing from approximately −0.257 V to −0.269 V (vs. Ag/AgCl) over 2190 s. Subsequently, the behavior transitions to cathodic, characterized by a slow potential rise toward stabilization. The OCP behavior is governed by a dynamic equilibrium between the anodic exchange oxidation current (i_{oa}) and the cathodic exchange reduction current (i_{oc}) under open-circuit conditions, as described by Equation 1, which is deduced from the Butler-Volmer relationship under non-equilibrium conditions[14]:

$$E_{OC} = E_{eq} + \frac{RT}{nF}\ln\left(\frac{i_{oc}}{i_{oa}}\right) \quad (1)$$

where $E_{eq} = E_{eq,c} + \beta E_{eq,a}$ represents the equilibrium potential of the combined anodic and cathodic reactions.

The initial potential decrease indicates the predominance of the anodic current ($i_{oa} > i_{oc}$), suggesting relative corrosion of the Ni phase, since the starting E_{OC} (~−0.257 V vs. Ag/AgCl) is less negative than the Ni redox potential. This initial potential drop could also associate with the corrosion of the priory formed Ni-O based oxides, which was predicted by the Pourbaix diagram[15] and reported for some researchers[16]. However, this corrosion trend is counteracted by the competing passivation of silicon, which forms SiO_2 due to its less negative redox potential (< −0.47 V vs. SHE). During this process, Cl^- ions act as dissolution agents for both Ni and SiO_2, leading to pit formation on the electrode surface. For immersion times exceeding 2190 s, the E_{OC} gradually recovers ($i_{oa} < i_{oc}$), as seen in Figure 4. This change may be attributed to the formation of a passivating WO_3 layer (Equation 2) or WO_4^{2-} species (Equation 3), along with the presence of carbon-based compounds.

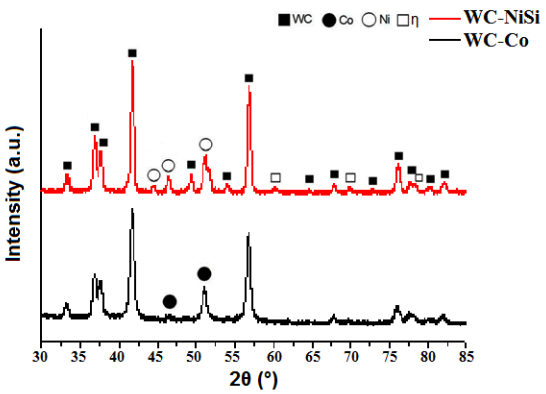

Figure 3. XRD of the WC-Co and WC-NiSi cemented carbides.

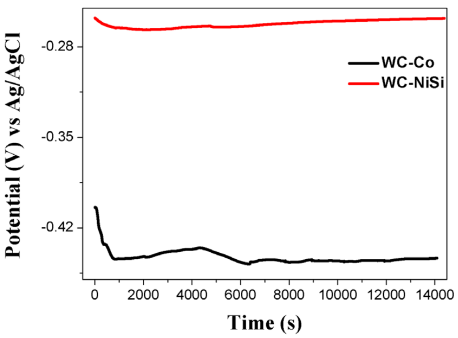

Figure 4. Variation of open circuit potential as a function of time for the WC-Co and WC-NiSi cemented carbides in 3.5% NaCl solution and room temperature.

Table 2. Chemical compositions of WC-Co and WC-NiSi cemented carbides obtained by EDS.

Sample	Chemical composition (wt. %)					
	W	C	O	Co	Ni	Si
WC-Co	80.32	9.48	1.19	9.00	-	-
WC-NiSi	77.63	6.86	1.15	-	14.33	0.03

$$WC + 5H_2O \rightarrow WO_3 + CO_2 + 10H^+ + 8e^- \quad (2)$$

$$WC + 3CO_3^{2-} + 6H_2O \rightarrow WO_4^{2-} + 3HCO_3^- + CO_2 + 9H^+ + 8e^- \quad (3)$$

For the WC-Co sample, Figure 4 reveals an abrupt initial E_{OC} shift to ≈−0.403 V vs Ag/AgCl at $t = 0$ s, followed by a sharp drop to −0.444 V vs Ag/AgCl within the first 1157.6 s. This decline is nearly four times faster than observed in the WC-NiSi sample, indicating significantly higher reactivity—consistent with materials exhibiting low corrosion resistance. The initial corrosion is primarily attributed to Co dissolution, facilitated by the E_{OC} being less negative than the redox potential of the Co/Co^{2+} reaction (−0.474 V vs Ag/AgCl) alongside possible dissolution of preformed oxides. This process likely exposes the more electrochemically active binder phase, further driving the E_{OC} decrease. As with the WC-NiSi sample, Cl^- ions play a critical role in pit formation. Subsequently, the E_{OC} profile reflects a dynamic competition between passivating cathodic reactions and ongoing corrosion, eventually stabilizing near −0.444 V vs Ag/AgCl. In contrast, the WC-NiSi cemented carbide exhibited a more noble potential (E_{OC} = −0.26 V vs Ag/AgCl), as expected, given nickel's superior corrosion resistance compared to cobalt (E_{OC} = −0.444 V vs Ag/AgCl). This stability is further enhanced by the presence of Si, which reduces surface corrosion through the possible formation of soluble $SiCl_4$ complexes.

3.2.2. Polarization

Figure 5 shows the polarization curves of the WC-Co and WC-NiSi cemented carbides after one hour of immersion. It is noted that the shape of the polarization curve of the sample with nickel binder presents behavior quite similar to that of cobalt, both in the cathodic and anodic sections, and does not significantly change the shape of the curve. In the cathodic branch, for both samples, the curves present a section with a gentler slope, similar to a plateau. This behavior indicates a dominance of the oxygen reduction reaction ($O_2 + 2H_2(l) + 4e- \rightarrow 4OH-(aq)$)[13,17]. In addition, the higher anodic current exhibited for WC-Co is coherent with its less corrosion resistance surface, as anticipated by the E_{OC} analysis.

For the anodic section of the curves, the current density initially increases exponentially as the potential is increased above the corrosion potential, E_{corr}, indicating a control by activation in this region, caused by the dissolution of the binder phase[18]. The process continues until a peak of maximum/critical current densityis reached, after which the materials show a reduction in current and then develop a nearly stable and relatively potential-independent plateau. Although this behavior is similar to the passivation phenomenon, it is called pseudo-passivation, because despite the decrease in current, it remains at levels much higher than the values of typical passivation, which occurs when the current density is less than 10 μA/cm² [19].

For potentials higher than those of the pseudo-passive section, the current density begins to increase rapidly again with the increase in potential, similar to typical transpassive behavior, after which the current does not show great variation, remaining relatively stable. This rise in current density results from WC oxidation. While selective dissolution of the binder dominates at open-circuit conditions or low applied potentials, higher potentials also induce carbide dissolution[16,20].

Sutthiruangwong et al.[21] attribute two reasons for pseudo-passivity. The first is caused by the limitation of cobalt ion diffusion through the porous tungsten carbide skeleton formed after cobalt dissolution. The second occurs in cemented carbides with a high tungsten content in the binder, where corrosion products, such as tungsten oxides, can be formed on the surface of the binders and, therefore, decrease the dissolution rate by inhibiting further dissolution of the binder. For the WC-NiSi sample, it is likely that something similar to the second reason mentioned above occurred, as it exhibits behavior similar to that of the WC-Co sample. As observed in the work of Pereira et al.[22], in the case of the sample with a nickel-based binder, higher overpotentials had to be applied to achieve similar current densities. Since nickel has superior corrosion resistance compared to cobalt, this may have contributed to the reduction in current density and the widening of the pseudo-passive range in the polarization curves.

Table 3 presents the electrochemical parameters derived from the potentiodynamic polarization curves (Figure 5).

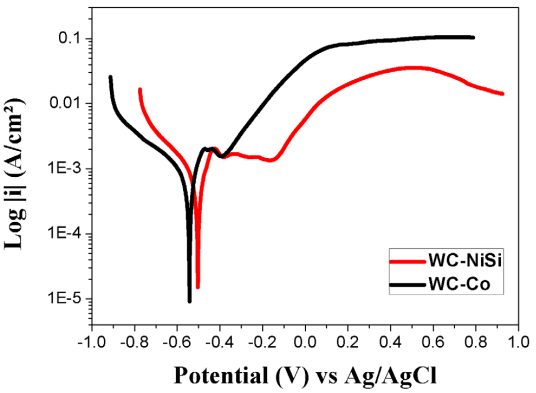

Figure 5. Linear potentiodynamic polarization curves of WC-Co and WC-NiSi Cemented carbides in 3.5% NaCl solution and room temperature.

Table 3. Electrochemical parameters for the WC-Co and WC-NiSi cemented carbides in 3.5% NaCl solution and room temperature.

Sample	i_{corr} (μA/cm²)	E_{corr} (V)	i_{crit} (μA/cm²)	$i_{min,pp}$ (μA/cm²)
WC-NiSi	828.40	-0.50	2033.52	1339.66
WC-Co	3315.80	-0.54	2021.50	1549.92

The corrosion potential (E_{corr}) and E_{OC} reflect the thermodynamic stability of the samples. Higher E_{corr} values typically indicate greater chemical stability and lower corrosion susceptibility in the tested electrochemical system[19,23]. Consistent with the E_{OC} trends, Table 3 shows that the nickel sample exhibits a more noble E_{corr} than the cobalt sample.

The corrosion current density (i_{corr}), which reflects the kinetics of corrosion, exhibits an inverse correlation with corrosion resistance. As shown in Table 3, the sample with the nickel binder exhibits an i_{corr} value approximately four times lower than that of the sample with the cobalt binder. Given that the corrosion rate is typically proportional to i_{corr}—alongside the observed shifts in Ecorr—this further confirms the enhanced corrosion resistance achieved by replacing cobalt with nickel[23,24,25].

For the WC-NiSi sample, the critical current density value is 2033.52 μA/cm^2, a value very close to that found for the sample with cobalt binder, falling to a minimum value of 1339.66 μA/cm^2 in the pseudo-passivity region. Although there is no sharp drop in current density in the pseudo-passivity region, and the material still presents current values much higher than those of a material that undergoes passivation, the sample presented a reduction in current density in practically all anodic region and an expansion in the pseudo-passivity range (from −0.43 V to −0.16 V) in relation to the cobalt sample (from −0.47 V to −0.38 V).

3.2.2.1. Microstructural analysis after polarization

Figures 6 and 7 show the micrographs of the WC-Co and WC-NiSi samples after the polarization test. In the WC-Co sample, no corrosion is observed on the WC particles and the corrosion process develops through the selective dissolution of the binder phase in the corrosive medium, the corrosion extends laterally and the dissolution of all the cobalt binder on the sample surface occurs, forming elongated pores with non-regular geometry.

For the WC-NiSi sample, no sign of corrosion was observed in the WC particles and the corrosion developed through the formation of pits or in pores already existing in the material. However, unlike the WC-Co sample, the dissolution of the binder did not propagate laterally, forming isolated pores with almost circular shape. The pit formation on both samples was anticipated from the E_{OC} analysis (Figure 4).

The polarization test results indicate that the cobalt-based sample exhibited the highest current density values among the tested samples. As shown in Table 4, the Co content in this sample was relatively low, suggesting that the WC-Co sample underwent the most significant reduction in binder content. This reduction is attributed to the selective dissolution of the cobalt binder phase.

The sample with nickel binder, as expected, presented higher binder contents and the sharp drop observed for the cobalt sample did not occur. However, as previously mentioned, these values are not very reliable because tungsten fluorescence influences the quantification of other elements, mainly nickel and chromium[12].

In the chemical composition result for the WC-NiSi sample, the alloying element added to the sample also appears. However, silicon appears only as a trace, probably because of the difficulty in analyzing low atomic number elements such as carbon, oxygen, aluminum and silicon by EDS. However, it is worth noting that EDS analysis presents difficulty in identifying small variations in composition when the elements present are in concentrations below 5% by volume[10].

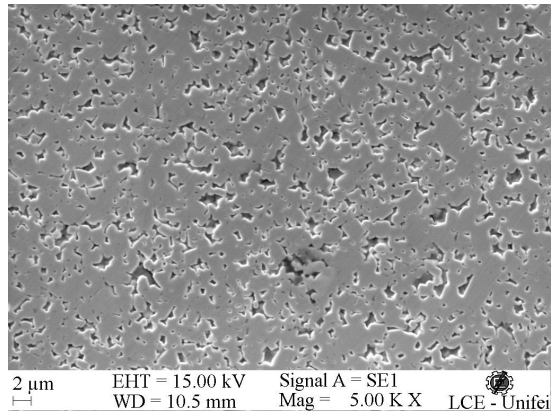

Figure 6. SEM image after polarization analysis in 3.5% NaCl solution at room temperature of WC–CO cemented carbide.

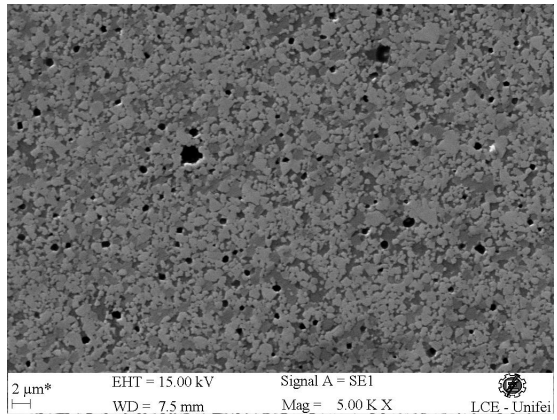

Figure 7. SEM image after polarization analysis in 3.5% NaCl solution at room temperature of WC–NiSi cemented carbide.

Table 4. Chemical compositions of WC-Co and WC-NiSi cemented carbides obtained by EDS, after polarization analysis in 3.5% NaCl solution.

Sample	Chemical composition after polarization test (wt. %)					
	W	C	O	Co	Ni	Si
WC-Co	90.23	8.47	1.07	0.24	-	-
WC-NiSi	77.03	6.26	1.46	-	15.25	0.00

Figure 8 shows the X-ray diffractograms (XRD) of the WC-Co and WC-NiSi cemented carbides after the potentiodynamic polarization test. Only the presence of peaks from the WC and nickel phases is observed, while the peaks from the cobalt and η phases visualized before the polarization test are no longer verified, suggesting the dissolution of these phases. The absence of Co is consistent with its strong corrosion tendency attributed to its more negative E_{OC} and almost sharp drop to -0.444V vs Ag/AgCl (Figure 4).

As anticipated, the diffraction peaks corresponding to the hard WC phase exhibit higher intensity and prevalence across all samples, reflecting its microstructural dominance and the selective dissolution of the binder phase. Notably, in the WC-Co sample, only WC peaks are detected after corrosion, with no residual Co signals—confirming severe binder degradation.

For the WC-NiSi sample, two Ni-binder phase peaks persist, though their intensity relative to WC is notably diminished, indicating partial dissolution. No oxide-related peaks were identified in the corrosion products, suggesting their concentrations fall below the detection threshold of the technique[26]. This aligns with EDS results, which revealed minimal oxygen content. However, Fan et al.[27] report that the primary corrosion products of WC-6Co in NaCl solution include $Co(OH)_2$, Co_3O_4, and trace WO_3, implying minor WC phase corrosion following Co-binder dissolution. Similarly, Farahmand and Kovacevic[16] observed NiO, Ni_2O_3, and WO_3 formation in a WC-40Ni coating exposed to 3.5 wt% NaCl.

3.2.3. Electrochemical impedance spectroscopy

The results of the impedance spectra of the samples in the form of Nyquist and Bode diagrams, measured at open circuit potential, are presented in Figures 9 and 10.

The Nyquist diagram provides an initial estimate of the solution resistance (R_s) at the intersection of the high-frequency region with the real impedance axis. The diameter of the semicircle corresponds to the load transfer resistance (R_{ct}), where a larger diameter indicates higher corrosion resistance and, consequently, a lower corrosion rate[28-30]. As shown in the diagram, the nickel-containing sample exhibits a larger semicircle diameter, suggesting greater R_{ct} compared to the WC-Co sample. This observation aligns with the findings from both the open-circuit potential (Figure 4) and polarization (Figure 5) analyses.

The Nyquist plots display purely capacitive semicircles confined to the first quadrant, indicating resistive behavior with no inductive response. The presence of these semicircles in the high-frequency region confirms that the corrosion process is governed by load transfer kinetics[26,31]. Since R_{ct} is inversely related to the I_{corr}, it serves as a direct indicator of corrosion resistance in activation-controlled systems[24], further supporting its correlation with corrosion rate.

The depressed semicircles observed in the Nyquist plot are an indication of multiple processes in the system and are commonly found in the semicircles corresponding to load transfer processes, mainly caused by non-uniform current distribution, roughness and porosity in the electrode. The resulting impedance of the semicircle is represented by a load transfer resistance in parallel with a constant phase element, Q_{CPE}. The constant phase element (CPE) can be represented by Equation 4[28]:

$$Z_{CPE} = \frac{1}{Q_{CPE}(j\omega)^n} \quad (4)$$

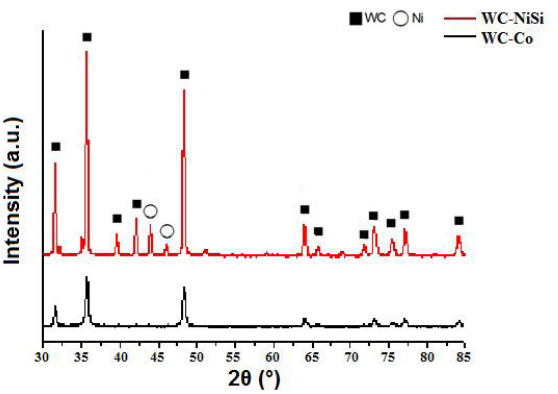

Figure 8. XRD of WC-Co and WC-NiSi cemented carbides, after polarization analysis in 3.5% NaCl solution.

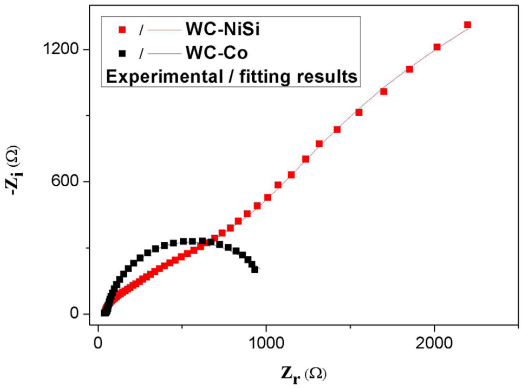

Figure 9. Nyquist diagram for the WC-Co (black symbols) and WC-NiSi (red symbols) cemented carbides in 3.5% NaCl solution at room temperature.

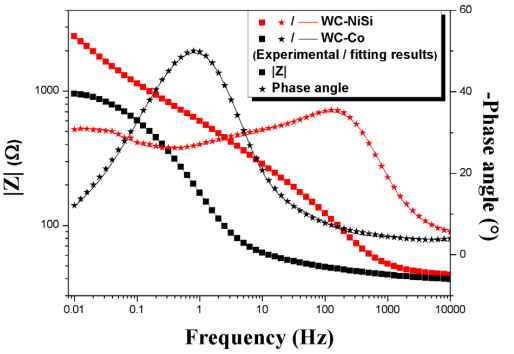

Figure 10. Bode modulus diagram (left axis – square symbols) and Bode phase diagram (right axis – star symbols) for the WC-Co and WC-NiSi cemented carbides in 3.5% NaCl solution at room temperature.

where ω is the angular frequency and n and Q_{CPE} are frequency-independent parameters related to the capacitive character of the system. The exponent n can assume values in the range $0 < n < 1.0$. When n = 1 and Q = C, the equation describes the impedance of an ideal capacitor. If n = 0, the equation provides the impedance response of an ideal resistor with Q = 1/R [32].

The Bode plot in Figure 10 reveals that the sample with a nickel binder exhibited higher total impedance across the entire frequency range compared to the sample with a cobalt binder, indicating greater corrosion resistance in the studied environment.

However, interpreting electrochemical systems using Bode plots presents challenges, particularly due to the influence of electrolytic resistance, which obscures the behavior of the electrode surface. To address this, modifying the Bode plots by subtracting the electrolyte resistance from the real part of the impedance can provide clearer insights into CPE behavior. Yet, inaccurate determination of electrolyte resistance may introduce significant errors. An alternative approach involves plotting the imaginary part of the impedance against frequency, as it remains unaffected by electrolyte resistance. In such plots, the slope remains constant, with its value equal to $-n$. As shown in Figure 11, the samples exhibit at least three distinct slopes, each with a value below 1, suggesting the presence of at least three CPE behaviors in all samples[33,34].

Figure 10 shows the Bode phase angle vs frequency plot. The WC-Co sample exhibits a single broad and undistorted peak, whereas the nickel-binder sample displays three consecutive broad peaks, with the peak between 0.1 and 10 Hz being notably lower in magnitude. A key observation is the widening of the phase angle in the nickel-containing sample, which correlates with enhanced corrosion resistance[34,35].

For a more in-depth investigation of the impedance data, they were fitted to an equivalent electrical circuit (EEC) model. Although such models aim to provide the best possible match to the experimental data, it is important to recognize that EIS represents a complex interaction of chemical, physical, electrical, and mechanical processes in purely electrical terms. Consequently, the EEC must incorporate circuit elements that reflect the underlying physical phenomena of the system under study[28].

In this regard, while Nyquist plots are effective in identifying basic circuit components (e.g., resistors, capacitors, and inductors), many electrode processes – particularly in electrochemical systems – are more complex than those represented in Figure 9. Graphical analysis alone is insufficient for such systems due to complexities such as the electrode-solution interface, electrochemical reactions, and mass transport[32]. Therefore, after evaluating the microstructures, impedance spectra, prior findings, and multiple circuit models, the EEC shown in Figure 12 was selected to numerically fit the experimental data.

In the proposed equivalent circuit [R([R([R(RQ)]Q)]Q)], R_s represents the resistance of the electrolyte solution between the sample surface (working electrode, WE) and the reference electrode (RE), as well as the resistance associated with the conductive wires connected to the electrodes. Given that the WE surface is covered by a pseudopassive oxide film, the contribution of this film to the EIS response was accounted for by incorporating a resistance (R_o), while its capacitive effect is represented by a CPE (Q_o). On the other hand, since the sample surface exhibits pores and pits, as revealed in Figures 1 and 2, the presence of these pores alters the local electric field distribution, thereby modifying all charge transfer processes compared to a planar surface. This effect was regarded by assigning a pore resistance (R_p) along with a constant phase element (Q_p) which describes the capacitive contribution of this region to the total impedance. Finally, R_{ct} represents the charge transfer resistance associated with the electrochemical processes taking place at the electrode-electrolyte interface, while Q_{dl} is a constant phase element that accounts for the electric double-layer capacitance at the sample-solution interface. The presence of these components corresponds to three distinct time constants, as evidenced in the WC-NiSi sample by three well-defined regions in the Bode phase plot (Figure 10), where peaks are observed near 0.01, 10, and 100 Hz. In contrast, these peaks appear overlapped in the WC-Co sample.

The parameters of the equivalent circuit elements, calculated using the NOVA program, are summarized in Table 5 (see Figure 12). Figures 9 and 10 display the Bode and Nyquist plots, comparing the experimentally obtained data with the simulated results from the equivalent circuit. The graphs demonstrate good agreement between the simulated and experimental data.

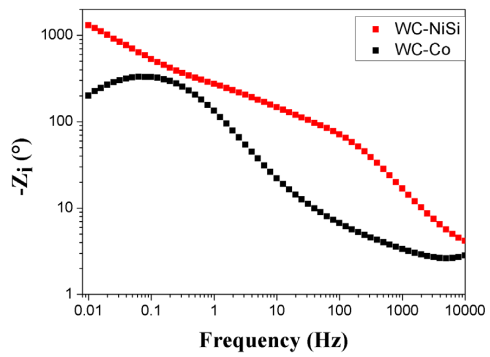

Figure 11. Modified Bode diagram for the WC-Co and WC-NiSi cemented carbides in 3.5% NaCl solution at room temperature.

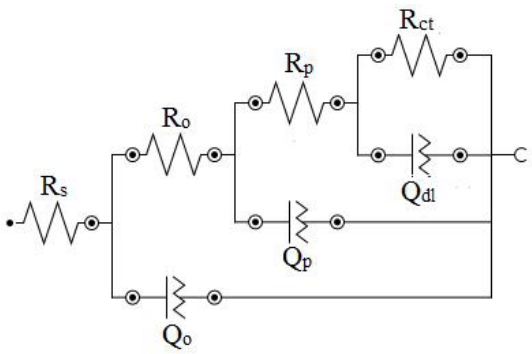

Figure 12. Equivalent electrical circuit used to numerically fit the experimental spectra.

Table 5. Electrochemical parameters of the WC-Co and WC-NiSi cemented carbides calculated by equivalent circuit simulation.

	WC-Co	WC-NiSi
R_s (Ω)	35.27	30.05
R_o (Ω)	15.46	26.18
Q_o ($\mu\Omega^{-1}S^n$)	933.58	766.52
n_o	0.48	0.36
R_p (Ω)	28.11	3331.7
Q_p ($\mu\Omega^{-1}S^n$)	315.58	5.47
n_p	0.91	0.99
R_{ct} (Ω)	1149	10517
Q_{dl} ($\mu\Omega^{-1}S^n$)	470.51	1143.7
n_{dl}	0.96	0.85

As shown in Table 5, the sample with the nickel binder exhibited higher resistance parameters and, in most cases, lower admittance values compared to the cobalt-based sample. Consequently, the nickel sample demonstrated greater capacitive impedance, aligning with the trends observed in the total impedance Bode diagram (Figure 10). Moreover, Table 5 reveals unexpected variations in the Rs values. This behavior may be attributed to the fact that Rs reflects the resistance induced by corrosion product films, which is higher in the WC-NiSi sample[19].

R_{ct} is the most critical parameter in this analysis, as it directly correlates with corrosion rate, as earlier commented. A higher R_{ct} indicates greater corrosion resistance and, thus, a slower corrosion rate[36]. The nickel binder sample exhibited a significantly higher R_{ct} value, confirming its superior corrosion resistance. This finding is consistent with the potentiodynamic polarization test results, where the nickel sample displayed a corrosion current density one order of magnitude lower than that of the cobalt sample.

4. Conclusions

Samples of WC-NiSi and WC-Co were prepared and characterized to evaluate their corrosion resistance. In the open circuit potential electrochemical test, the sample with nickel binder exhibited a more noble potential than that of WC-Co. During the potentiodynamic polarization tests, the WC-NiSi sample displayed behavior similar to WC-Co, though with a slight shift toward more noble potentials. Post-polarization microstructural characterization revealed selective binder dissolution as the primary corrosion mechanism in both samples. However, the WC-NiSi sample exhibited a distinct corrosion morphology compared to WC-Co, as its binder dissolution did not propagate laterally.

Electrochemical impedance spectroscopy further confirmed the superior corrosion resistance of the nickel-based binder in the tested medium. The WC-NiSi sample demonstrated higher total impedance across the entire frequency range compared to the cobalt-based sample.

Overall, the WC-NiSi sample exhibited the best corrosion resistance, as evidenced by its optimal performance in all electrochemical tests, including the most noble electrochemical behavior in the studied environment. Consequently, WC-NiSi emerges as the most suitable material for applications in the tested solution.

5. Acknowledgements

The authors are grateful for the valuable financial support of FAPEMIG, CAPES and CNPq.

6. References

1. Kai-Hua S, Ke-Chao Z, Zhi-You L, Xiu-Qi Z, Shang-Zhi X, Zhao-Yu M. Effect of adding method of Cr on microstructure and properties of WC–9Ni–2Cr cemented carbides. Int J Refract Met Hard Mater. 2013;38:1-6.
2. Torres CS, Schaeffer L. Effect of high energy milling on the microstruture and properties of Wc-Ni composite. Mater Res. 2010;13(3):293-8.
3. Correa EO, Santos JN, Klein AN. Microstructure and mechanical properties of WC-Ni-Si based cemented carbides developed by powder metallurgy. Int J Refract Met Hard Mater. 2010;28(5):572-5.
4. Human AM, Exner HE. Electrochemical behaviour of tungsten-carbide hardmetals. Mater Sci Eng A. 1996;209:180-91.
5. Calderon RO, Agna A, Gomes UU, Schubert WD. Phase formation in cemented carbides prepared from WC and stainless steel powder: an experimental study combined with thermodynamic calculations. Int J Refract Met Hard Mater. 2019;80:225-37.
6. Fernandes CM, Rocha A, Cardoso JP, Bastos AC, Soares E, Sacramento J, et al. WC-stainless steel hardmetals. Int J Refract Met Hard Mater. 2018;72:21-6.
7. Balbino NAN, Correa EO, Valeriano LC, Amâncio DA. Microstructure and mechanical properties of 90WC-8Ni-2Mo2C cemented carbide developed by conventional powder metallurgy. Int J Refract Met Hard Mater. 2017;68:49-53.
8. Zhao Z, Liu J, Tang H, Ma X, Zhao W. Effect of Mo addition on the microstructure and properties of WC–Ni–Fe hard alloys. J Alloys Compd. 2015;646:155-60.
9. Marques BJ, Fernandes CM, Senos AMR. Sintering, microstructure and properties of WC-AISI304 powder composites. J Alloys Compd. 2013;562:164-70.
10. Bezerra RM. Estudo de solda a laser em ligas odontológicas utilizadas em próteses sobre implantes: Titânio comercialmente puro e liga de ouro. [dissertation]. São Carlos: Universidade de São Paulo, Escola de Engenharia de São Carlos; 1999.
11. Milheiro FAC. Produção e caracterização de pós compósitos nanoestruturados do metal duro WC-10Co por moagem de alta energia. [dissertation]. Campos dos Goytacazes: Universidade Estadual do Norte Fluminense; 2006.
12. Fernandes CMS. Caracterização e processamento de pós de carboneto de tungsténio revestido com aço inoxidável. [dissertation]. Aveiro: Universidade de Aveiro; 2002.
13. Liberto RCN. Corrosão e propriedades mecânicas de ligas cuproníquel 90-10 com adição de ferro e alumínio. [dissertation]. São Paulo: Universidade de São Paulo, Escola Politécnica; 2004.
14. Gileadi E. Physical electrochemistry. Weinheim: Wiley-VHC; 2013.
15. Pourbaix M. Electrochemical equilibria in aqueous solutions. Houston: National Association of Corrosion Engineers; 1974.
16. Farahmand P, Kovacevic R. Corrosion and wear behavior of laser cladded Ni–WC coatings. Surf Coat Tech. 2015;276:121-35.
17. Habibi Rad M, Ahmadian M, Golozar MA. Investigation of the corrosion behavior of WC–FeAl–B composites in aqueous media. Int J Refract Met Hard Mater. 2012;35:62-9.
18. Human AM, Exner HE. The relationship between electrochemical behaviour and in-service corrosion of WC based cemented carbides. Int J Refract Met Hard Mater. 1997;15(1–3):65-71.

19. Han B, Dong W, Bai Y, Ding H, Luo Y, Di P. Electrochemical corrosion behavior of hot-pressing sintered WC-Al2O3 composite in alkaline and acidic solutions. J Mater Sci. 2021;56(6):4120-34.
20. Silva FS, Cinca N, Dosta S, Cano IG, Couto M, Guilemany JM, et al. Corrosion behavior of WC-Co coatings deposited by cold gas spray onto AA 7075-T6. Corros Sci. 2018;136:231-43.
21. Sutthiruangwong S, Mori G, Kösters R. Passivity and pseudopassivity of cemented carbides. Int J Refract Met Hard Mater. 2005;23:129-36.
22. Pereira P, Vilhena L, Sacramento J, Senos A, Malheiros L, Ramalho A. Influence of different binders and severe environmental conditions on the tribological and electrochemical behaviour of WC-based composites. Lubricants. 2022;10(7):145.
23. Qiu W, Liu Y, Ye J, Fan H, Qiu Y. Effects of (Ti,Ta,Nb,W)(C,N) on the microstructure, mechanical properties and corrosion behaviors of WC-Co cemented carbides. Ceram Int. 2017;43(3):2918-26.
24. Revie RW, Uhlig HH. Corrosion and corrosion control: an introduction to corrosion science and engineering. New Jersey: John Wiley & Sons, Inc.; 2008.
25. Zhang L, Chen Y, Feng Y, Chen S, Wan Q, Zhu J. Electrochemical characterization of AlTiN, AlCrN and AlCrSiWN coatings. Int J Refract Met Hard Mater. 2015;53:68-73.
26. Ahmed R, Vourlias G, Algoburi A, Vogiatzis C, Chaliampalias D, Skolianos S, et al. Comparative study of corrosion performance of HVOF-sprayed coatings produced using conventional and suspension WC-Co feedstock. J Therm Spray Tech. 2018;27(8):1579-93.
27. Fan B, Zhu S, Dong W, Ding H, Bai Y, Luo Y, et al. Comparative study on corrosion behavior of WC-MgO composite and WC-6Co cemented carbide in NaCl solution. Ceram Int. 2021;47(5):7106-16.
28. Lvovich VF. Impedance spectroscopy applications to electrochemical and dielectric phenomena. New Jersey: John Wiley & Sons, Inc.; 2012.
29. Ribeiro DV, Souza CAC, Abrantes JCC. Uso da Espectroscopia de Impedância Eletroquímica (EIE) para monitoramento da corrosão em concreto armado. Rev IBRACON Estrut Mater. 2015;8(4):529-46.
30. Wang X, Wang H, Liu X, Hou C, Song X. Microstructure and performance of WC–Co–Cr coating with ultrafine/nanocrystalline structures. Rare Met. 2018;37(11):968-75.
31. Brioua S, Belmokre K, Debout V, Jacquot P, Conforto E, Touzain S, et al. Corrosion behavior in artificial seawater of thermal-sprayed WC-CoCr coatings on mild steel by electrochemical impedance spectroscopy. J Solid State Electrochem. 2012;16:633-48.
32. Ribeiro J. Electrochemical impedance spectroscopy: a tool on the electrochemical investigations. Rev Virtual Quim. 2020;12(6):1626-41.
33. Jorcin JB, Orazem ME, Pébère N, Tribollet B. CPE analysis by local electrochemical impedance spectroscopy. Electrochim Acta. 2006;51(8–9):1473-9.
34. Fazili A, Derakhshandeh MR, Nejadshamsi S, Nikzad L, Razavi M, Ghasali E. Improved electrochemical and mechanical performance of WC-Co cemented carbide by replacing a part of Co with Al2O3. J Alloys Compd. 2020;823:153857.
35. Kellner FJJ, Hildebrand H, Virtanen S. Effect of WC grain size on the corrosion behavior of WC–Co based hardmetals in alkaline solutions. Int J Refract Met Hard Mater. 2009;27:806-12.
36. Rocha AMF, Bastos AC, Cardoso JP, Rodrigues F, Fernandes CM, Soares E, et al. Corrosion behaviour of WC hardmetals with nickel-based binders. Corros Sci. 2019;147:384-93.

Data Availability

The datasets generated during the current study are not publicly available, but can be obtained from the corresponding author on reasonable request.